Subspace Migration for Imaging of Thin Electromagnetic Inhomogeneities without Shape Information

W.-K. Park
Department of Mathematics, Kookmin University, Seoul 136-702, Korea

Abstract— Subspace migration is a stable and effective non-iterative imaging technique for approaching the inverse scattering problem. However, for the successful imaging of thin electromagnetic inhomogeneities, *a priori* information about tangential and normal directions to unknown targets must be known. If this *a priori* information is not known, good results cannot be obtained using subspace migration. For this reason, various test vectors are applied to the imaging functional. However, this involves large computational costs, and the results may still be poor. With this as motivation, we derive the structure of single-frequency subspace migration, without any knowledge of shape information for unknown targets, and explore some properties thereof. This is based on the fact that measured far-field can be written as an asymptotic expansion formula. Some numerical results are then demonstrated, in support of our derivation.

1. INTRODUCTION

One point of view holds that the main purpose of the inverse scattering problem is to identify unknown characteristics of an object (such as its shape or material properties), using scattered field data. As a result of much research, various algorithms for reconstructing the shape of thin electromagnetic inhomogeneities or perfectly conducting cracks have been suggested, based mostly upon Newton-type iteration schemes or the level set method. Further details can be found in [1, 7, 13] and references therein. However, in order for these schemes to be successfully applied, a good initial guess is essentially required. Without that, one might encounter large computational costs, non-convergence issues, and the occurrence of local minimizer problems. Moreover, iterative schemes often require regularization terms that strongly depend on the problem at hand. Therefore, many authors have suggested the use of non-iterative reconstruction algorithms, which could at least provide good initial guesses. Further details are given in [2–4, 6, 8, 9, 11, 12].

Among such methods, subspace migration algorithm has been shown to be feasible for imaging applications. However, for the assurance of good results for the imaging of thin inhomogeneities, *a priori* information must be known about tangential and normal vectors on the boundaries (see [8, 9] for instance). As a result, many authors have applied a suitable vector to the subspace migration to consider the subspace migration without having any information about unknown targets. Motivated by this fact, we establish a relationship between single-frequency subspace migration and Bessel functions of the first kind of integer order. This is based on the fact that the far-field pattern can be represented as an asymptotic expansion formula in the presence of a thin electromagnetic inhomogeneity, refer to [5]. This relationship lets us uncover certain properties of subspace migration, and it can be applied successfully without knowing any information about a thin inhomogeneity.

This paper is organized as follows. In Section 2, we briefly introduce the two-dimensional direct scattering problem and subspace migration. In Section 3, we explore the structure of subspace migration, without consideration of the shape of thin inhomogeneities. In Section 4, we exhibit some results of numerical simulations with noisy data. A brief conclusion follows in Section 5.

2. THE DIRECT SCATTERING PROBLEM AND SUBSPACE MIGRATION

2.1. A Two-dimensional Direct Scattering Problem for a Thin Electromagnetic Inhomogeneity

Assume an extended, penetrable electromagnetic inhomogeneity Γ, with a small (with respect to the given wavelength) thickness of $2h$, is located in the two-dimensional homogeneous space $\mathbb{R}^2$. That is,

$$\Gamma = \{\mathbf{x} + \eta\mathbf{n}(\mathbf{x}) : \ \mathbf{x} \in \sigma, \ -h \le \eta \le h\},$$

where $\mathbf{n}(\mathbf{x})$ is the unit normal to σ at x, and σ denotes a simple, smooth curve in $\mathbb{R}^2$, describing the supporting curve of Γ. In this paper, we assume that Γ and $\mathbb{R}^2$ are characterized by their dielectric permittivities and magnetic permeabilities at a given angular frequency $\omega = 2\pi/\lambda$, where λ denotes the wavelength. Let ε_0 and $\varepsilon_\star$ be the dielectric permittivity of $\mathbb{R}^2$ and Γ, respectively; μ_0 and $\mu_\star$ are defined similarly. For the sake of simplicity, we set $\varepsilon_0 = \mu_0 \equiv 1$.

At a given ω, we denote by $u_\circ(\mathbf{x}) := \exp(i\omega\theta \cdot \mathbf{x})$ a plane-wave incident field with incident direction $\theta \in \mathbb{S}^1$, where $\mathbb{S}^1$ denotes the unit circle. Let $u(\mathbf{x})$ be the time-harmonic total field that satisfies the Helmholtz equation

$$\nabla \cdot \left(\frac{1}{\mu_\star}\chi(\Gamma) + \frac{1}{\mu_0}\chi\left(\mathbb{R}^2 \backslash \overline{\Gamma}\right)\right) \nabla u(\mathbf{x}) + \omega^2 \left(\varepsilon_\star \chi(\Gamma) + \varepsilon_0 \chi\left(\mathbb{R}^2 \backslash \overline{\Gamma}\right)\right) u(\mathbf{x}) = 0 \quad \text{in} \quad \mathbb{R}^2, \tag{1}$$

with a transmission condition on the boundary of Γ. Then, $u(\mathbf{x})$ can be decomposed as $u(\mathbf{x}) = u_\circ(\mathbf{x}) + u_\diamond(\mathbf{x})$, where $u_\diamond(\mathbf{x})$ is the unknown scattered field that uniformly satisfies the Sommerfeld radiation condition

$$\lim_{|\mathbf{x}|\to\infty} \sqrt{|\mathbf{x}|}\left(\frac{\partial u_\diamond(\mathbf{x})}{\partial |\mathbf{x}|} - ik_0 u_\diamond(\mathbf{x})\right) = 0, \quad k_0 = \omega\sqrt{\varepsilon_0\mu_0} = \omega,$$

in all directions $\hat{\mathbf{x}} = \mathbf{x}/|\mathbf{x}|$.

The far-field pattern $u_\infty(\vartheta, \theta)$ of $u_\diamond(\mathbf{x})$ is defined on $\mathbb{S}^1$. Note that it is represented as

$$u_\diamond(\mathbf{x}) = \frac{\exp(i\omega|\mathbf{x}|)}{\sqrt{|\mathbf{x}|}} u_\infty(\vartheta, \theta) + o\left(\frac{1}{\sqrt{|\mathbf{x}|}}\right), \tag{2}$$

as $|\mathbf{x}| \to \infty$ uniformly on $\vartheta = \mathbf{x}/|\mathbf{x}|$. Then, $u_\infty(\vartheta, \theta)$ can be written in the form of the following asymptotic expansion formula:

$$u_\infty(\vartheta, \theta) = h\frac{\omega^2(1+i)}{4\sqrt{\omega\pi}} \int_\sigma \left(\frac{\varepsilon_\star - \varepsilon_0}{\sqrt{\varepsilon_0 \mu_0}} - \left(\sqrt{2}\vartheta\right) \cdot \mathbb{M}(\mathbf{x}) \cdot \left(\sqrt{2}\theta\right)\right) \exp\left(i\omega(\theta - \vartheta)\cdot \mathbf{x}\right) d\sigma(\mathbf{x}) + o(h), \tag{3}$$

where $o(h)$ is uniform in $\mathbf{x} \in \sigma$, and $\mathbb{M}(\mathbf{x})$ is a symmetric matrix (see [5] for instance).

2.2. Introduction to Subspace Migration

We introduce subspace migration for the imaging of Γ. For the sake of simplicity, suppose that we have a number N of different incident and observation directions, θ_l and ϑ_j respectively, for $j, l = 1, 2, \ldots, N$ and $\vartheta_j = -\theta_j$. Furthermore, suppose that the supporting curve σ is divided into M different segments, of sizes of the order of half the wavelength, $\lambda/2$. Then, considering the Rayleigh resolution limit for far-field data, any detail that is less than one half of the wavelength cannot be seen, and only one point from each segment is expected to contribute at the image space of the response matrix $\mathbb{K}$ (see [4, 9, 11, 12] for instance). Each of these points, say $\mathbf{x}_m$ for $m = 1, 2, \ldots, M$, will be imaged. With this in mind, we consider the collected MSR matrix, and perform Singular Value Decomposition (SVD) as follows:

$$\mathbb{K} = \left[u_\infty\left(\mathbf{x}_j, \theta_l\right)\right]_{j,l=1}^N = \mathbb{U}\mathbb{E}\mathbb{V}^* \approx \sum_{m=1}^{3M} \tau_m \mathbf{U}_m \mathbf{V}_m^*, \tag{4}$$

where the superscript $*$ denotes a complex conjugate, the τ_m are non-zero singular values, and $\mathbf{U}_m$ and $\mathbf{V}_m$ are the left- and right-singular vectors of $\mathbb{K}$, respectively. Based on (4), the imaging algorithm is developed as follows. For $\mathbf{c}_n \in \mathbb{R}^{3\times 1}\backslash\{\mathbf{0}\}$, $n = 1, 2, \ldots, N$, define a vector

$$\mathbf{W}(\mathbf{z}) := \frac{1}{N}\left[\mathbf{c}_1 \cdot [1, \theta_1]^T \exp(i\omega\theta_1 \cdot \mathbf{z}), \ldots, \mathbf{c}_N \cdot [1, \theta_N]^T \exp(i\omega\theta_N \cdot \mathbf{z})\right]^T. \tag{5}$$

Then, by virtue of results in [2, 8, 9], the following relationship holds:

$$\mathbf{W}(\mathbf{x}_m) \approx \mu_m \quad \text{and} \quad \mathbf{W}(\mathbf{x}_m) \approx \overline{\mathbf{V}}_m. \tag{6}$$

Hence, by the orthonormal property of singular values, we can observe that

$$\begin{aligned} \mathbf{W}(\mathbf{z})^*\mathbf{U}_m \approx 1 \quad &\text{and} \quad \mathbf{W}(\mathbf{z})^*\overline{\mathbf{V}}_m \approx 1 \quad \text{if} \quad \mathbf{z} = \mathbf{x}_m, \\ \mathbf{W}(\mathbf{z})^*\mathbf{U}_m \approx 0 \quad &\text{and} \quad \mathbf{W}(\mathbf{z})^*\overline{\mathbf{V}}_m \approx 0 \quad \text{if} \quad \mathbf{z} \neq \mathbf{x}_m. \end{aligned} \tag{7}$$

Therefore, we can introduce the subspace migration imaging functional as follows:

$$\mathcal{I}_{\mathrm{SF}}(\mathbf{z}) := \left| \sum_{m=1}^{3M} \left(\mathbf{W}(\mathbf{z})^*\mathbf{U}_m\right)\left(\mathbf{W}(\mathbf{z})^*\overline{\mathbf{V}}_m\right)\right|. \tag{8}$$

Based on (7), $\mathcal{I}_{\mathrm{SF}}$ is expected to exhibit peaks of a magnitude of 1 at $\mathbf{z} = \mathbf{x}_m \in \sigma$, and of small magnitudes at $\mathbf{z} \in \mathbb{R}^2\backslash\Gamma$.

3. STRUCTURE OF SUBSPACE MIGRATION WITHOUT SHAPE INFORMATION

Based on the above, the definition of a vector $\mathbf{W}(\mathbf{z})$ in (5) is very important for the performance of imaging. For this purpose, one must choose suitable vectors $\mathbf{c}_n$. Note that, following from (3) and (6), each $\mathbf{c}_n$ must be a linear combination of tangential $\mathbf{t}(\mathbf{x}_m)$ and normal $\mathbf{n}(\mathbf{x}_m)$ vectors at $\mathbf{x}_m \in \sigma$. However, when we have no *a priori* information about the shape of Γ, it is impossible to select an optimal vector $\mathbf{c}_n$, and therefore also an optimal $\mathbf{W}(\mathbf{z})$. Therefore, instead of (5), we choose an alternative test vector

$$\mathbf{W}(\mathbf{z}) := \frac{1}{N}\left[\exp(i\omega\theta_1 \cdot \mathbf{z}),\, \exp(i\omega\theta_2 \cdot \mathbf{z}),\, \ldots,\, \exp(i\omega\theta_N \cdot \mathbf{z})\right]^T. \tag{9}$$

Subsequently, the structure of subspace migration can be represented as follows. A detailed derivation is to appear in an extended version of this contribution.

Theorem 3.1. *For sufficiently large $N(> 3M)$ and ω, (8) can be represented as follows:*

$$\mathcal{I}(\mathbf{z}) = \left|\sum_{m=1}^{M}\left\{J_0\left(\omega|\mathbf{z}-\mathbf{x}_m|\right) + i\left(\frac{\mathbf{z}-\mathbf{x}_m}{|\mathbf{z}-\mathbf{x}_m|}\cdot(\mathbf{t}(\mathbf{x}_m)+\mathbf{n}(\mathbf{x}_m))\right)J_1\left(\omega|\mathbf{z}-\mathbf{x}_m|\right)\right\}^2\right|, \tag{10}$$

where J_n denotes the Bessel function of integer order n, of the first kind.

Proof. Considering (5) and (6), $\mathcal{I}(\mathbf{z})$ can be written as

$$\mathcal{I}(\mathbf{z}) = \left|\sum_{m=1}^{3M}\left(\mathbf{W}(\mathbf{z})^*\mathbf{U}_m\right)\left(\mathbf{W}(\mathbf{z})^*\overline{\mathbf{V}}_m\right)\right| \approx \left|\sum_{m=1}^{M}\left\{\sum_{s=1}^{3}\left(\mathbf{W}(\mathbf{z})^*\mathbf{H}_m^{(s)}\right)\right\}^2\right|,$$

where (see [10] for instance)

$$\begin{aligned}
\mathbf{H}_m^{(1)} &= \frac{1}{\sqrt{N}}\left[e^{i\omega\theta_1\cdot\mathbf{x}_m},\, e^{i\omega\theta_2\cdot\mathbf{x}_m},\, \ldots,\, e^{i\omega\theta_N\cdot\mathbf{x}_m}\right]^T,\\
\mathbf{H}_m^{(2)} &= \frac{1}{\sqrt{N}}\left[\theta_1\cdot\mathbf{t}(\mathbf{x}_m)e^{i\omega\theta_1\cdot\mathbf{x}_m},\, \theta_2\cdot\mathbf{t}(\mathbf{x}_m)e^{i\omega\theta_2\cdot\mathbf{x}_m},\, \ldots,\, \theta_N\cdot\mathbf{t}(\mathbf{x}_m)e^{i\omega\theta_N\cdot\mathbf{x}_m}\right]^T,\\
\mathbf{H}_m^{(3)} &= \frac{1}{\sqrt{N}}\left[\theta_1\cdot\mathbf{n}(\mathbf{x}_m)e^{i\omega\theta_1\cdot\mathbf{x}_m},\, \theta_2\cdot\mathbf{n}(\mathbf{x}_m)e^{i\omega\theta_2\cdot\mathbf{x}_m},\, \ldots,\, \theta_N\cdot\mathbf{n}(\mathbf{x}_m)e^{i\omega\theta_N\cdot\mathbf{x}_m}\right]^T.
\end{aligned}$$

Since for $\theta,\, \xi \in \mathbb{S}^1$ and $\mathbf{x} \in \mathbb{R}^2$ (see [9] for instance), we have that

$$\begin{aligned}
\frac{1}{N}\sum_{n=1}^{N}\exp(i\omega\theta_n\cdot\mathbf{x}) &= \frac{1}{2\pi}\int_{\mathbb{S}^1}\exp(i\omega\theta\cdot\mathbf{x})d\theta = J_0(\omega|\mathbf{x}|),\\
\frac{1}{N}\sum_{n=1}^{N}(\theta_n\cdot\xi)\exp(i\omega\theta_n\cdot\mathbf{x}) &= \frac{1}{2\pi}\int_{\mathbb{S}^1}(\theta\cdot\xi)\exp(i\omega\theta\cdot\mathbf{x})d\theta = i\left(\frac{\mathbf{x}}{|\mathbf{x}|}\cdot\xi\right)J_1(\omega|\mathbf{x}|),
\end{aligned}$$

we can perform some elementary calculus to obtain

$$\begin{aligned}
\mathbf{W}(\mathbf{z})^*\mathbf{H}_m^{(1)} &= J_0(\omega|\mathbf{z}-\mathbf{x}_m|),\\
\mathbf{W}(\mathbf{z})^*\mathbf{H}_m^{(2)} + \mathbf{W}(\mathbf{z})^*\mathbf{H}_m^{(3)} &= i\left(\frac{\mathbf{z}-\mathbf{x}_m}{|\mathbf{z}-\mathbf{x}_m|}\cdot(\mathbf{t}(\mathbf{x}_m)+\mathbf{n}(\mathbf{x}_m))\right)J_1\left(\omega|\mathbf{z}-\mathbf{x}_m|\right).
\end{aligned}$$

Hence, we can obtain (10). This completes the proof.

Based on the properties of $J_0(x)$, plots of $\mathcal{I}(\mathbf{z})$ will show peaks of magnitude 1 at $\mathbf{z} = \mathbf{x}_m \in \Gamma$, and smaller peaks at $\mathbf{z} \notin \Gamma$. It follows from the properties of $J_1(x)^2$ that two curves of large (but less than 1) magnitude, and many artifacts of smaller magnitude, will appear in the map of $\mathcal{I}(\mathbf{z})$.

4. RESULTS OF NUMERICAL SIMULATIONS

In this section, the results of some numerical simulations are exhibited in support of Theorem 3.1. For this purpose, thin inhomogeneities Γ_j and two supporting smooth curves are selected as follows:

$$\begin{aligned}
\sigma_1 &= \left\{\left[s-0.2,\, -0.5s^2+0.5\right]^T \;:\; -0.5 \le s \le 0.5\right\},\\
\sigma_2 &= \left\{\left[s+0.2,\, s^3+s^2-0.6\right]^T \;:\; -0.5 \le s \le 0.5\right\}.
\end{aligned}$$

We set the permittivities and permeabilities of Γ_j as 5, and those of $\mathbb{R}^2$ as 1. The thickness h of Γ_j is set to 0.015, and the wavelength λ is chosen as 0.5. Directions $\theta_l \in S^1$ are selected as

$$\theta_l = \left[\cos\frac{2\pi l}{N},\, \sin\frac{2\pi l}{N}\right]^T \quad \text{for} \quad l = 1, 2, \ldots, N.$$

In order to show the robustness of the result, a white Gaussian noise with 20 dB signal-to-noise ratio (SNR) is added to the unperturbed data $u_\infty(\vartheta_j, \theta_l)$.

Figure 1 shows the maps of $\mathcal{I}_{\mathrm{SF}}(\mathbf{z})$ with $\mathbf{c}_n = [1,1,0]^T$, $\mathbf{c}_n = [1,0,1]^T$, and $\mathcal{I}(\mathbf{z})$ for Γ_1. Note that since $\mathbf{n}(\mathbf{x}_m) \approx 1$ for all m, the selection of $\mathbf{c}_n = [1,0,1]^T$ yields good result but $\mathbf{c}_n = [1,1,0]^T$ is not a good choice. However, one can recognize the shape of Γ_1 via the map of $\mathcal{I}(\mathbf{z})$.

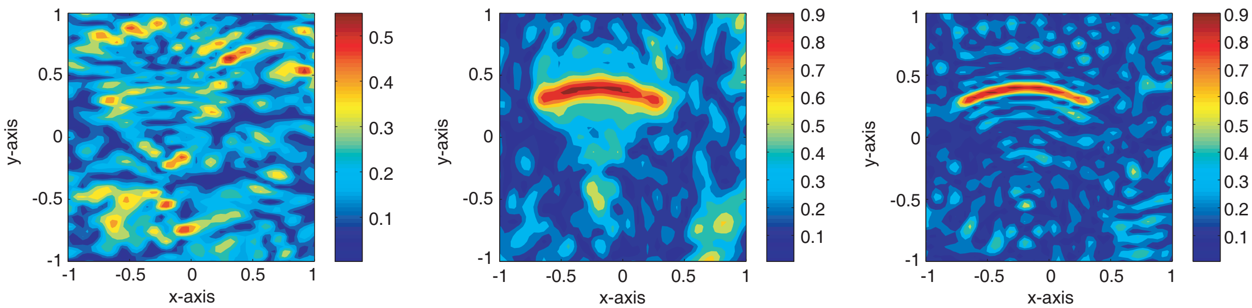

(a) (b) (c)

Figure 1: Maps of $\mathcal{I}_{\mathrm{SF}}(\mathbf{z})$ with (a) $\mathbf{c}_n = [1,1,0]^T$, (b) $\mathbf{c}_n = [1,0,1]^T$, and (c) $\mathcal{I}(\mathbf{z})$ for Γ_1.

Similar to Figure 1, Figure 2 shows the maps of $\mathcal{I}_{\mathrm{SF}}(\mathbf{z})$ and $\mathcal{I}(\mathbf{z})$, for Γ_2. In contrast to the previous result, the selection of $\mathbf{c}_n = [1,0,1]^T$ is no longer a good choice. Fortunately, the shape of Γ_2 is successfully reconstructed via the map of $\mathcal{I}(\mathbf{z})$.

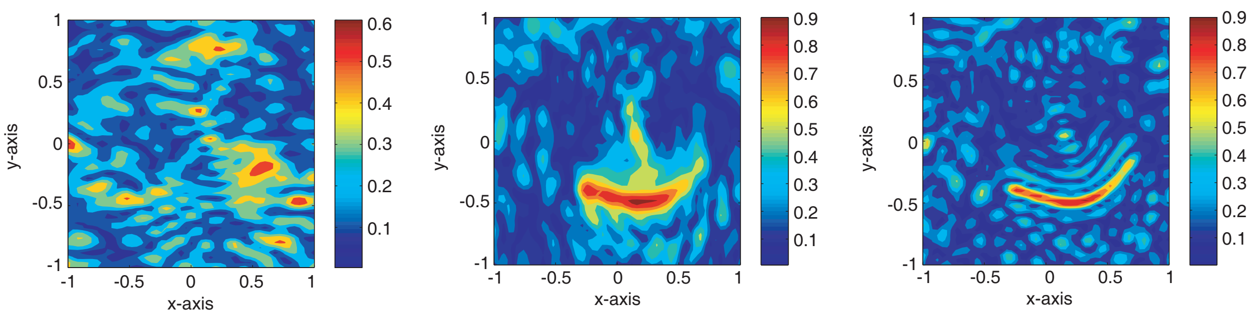

(a) (b) (c)

Figure 2: Similar to Figure 1, except the thin inhomogeneity, Γ_2.

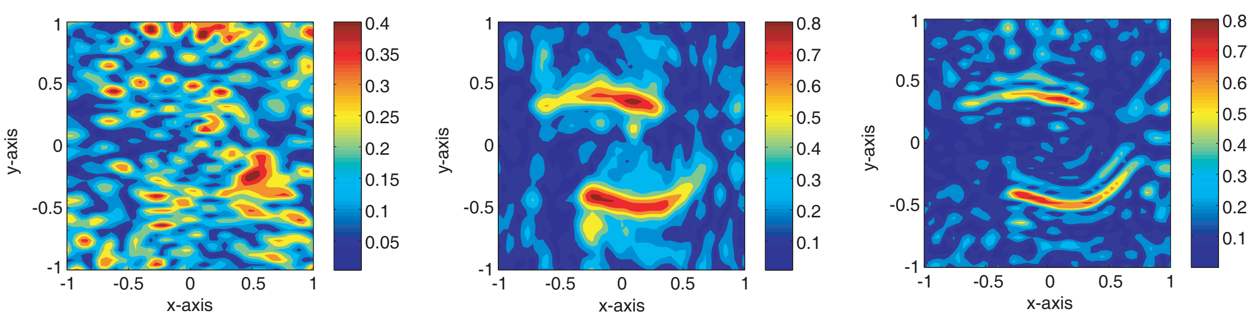

(a) (b) (c)

Figure 3: Similar to Figure 1, except the thin inhomogeneities, Γ_1 and Γ_2.

For the final example, let us consider the imaging results of multiple thin inhomogeneities $\Gamma_1 \cup \Gamma_2$. As with the previous results, we can observe that it is impossible to recognize the shape of $\Gamma_1 \cup \Gamma_2$

via the map of $\mathcal{I}_{\mathrm{SF}}(\mathbf{z})$ with $\mathbf{c}_n = [1, 1, 0]^T$. If one selects $\mathbf{c}_n = [1, 0, 1]^T$, the outline shape of $\Gamma_1 \cup \Gamma_2$ can be obtained, although the result is still poor. However, their shape can be successfully retrieved via the map of $\mathcal{I}(\mathbf{z})$.

5. CONCLUDING REMARKS

In this paper, we considered the subspace migration imaging functional without any information about the shape of thin inhomogeneities. We derived a relationship between the imaging functional and the Bessel functions of integer order of the first kind. The derived results indicated that although some unexpected artifacts still appear, we can obtain acceptable results using subspace migration without any consideration of the shape of unknown targets.

In the present work, we considered the imaging of thin electromagnetic inhomogeneities. Along the same lines, the analysis of subspace migration for the imaging of perfectly conducting cracks would make an interesting addition to this research.

ACKNOWLEDGMENT

This research was supported by Basic Science Research Program through the National Research Foundation of Korea (NRF) funded by the Ministry of Education (No. NRF-2014R1A1A2055225) and the research program of Kookmin University in Korea.

REFERENCES

1. Álvarez, D., O. Dorn, N. Irishina, and M. Moscoso, "Crack reconstruction using a level-set strategy," *J. Comput. Phys.*, Vol. 228, 5710–5721, 2009.
2. Ammari, H., J. Garnier, H. Kang, W.-K. Park, and K. Sølna, "Imaging schemes for perfectly conducting cracks," *SIAM J. Appl. Math.*, Vol. 71, 68–91, 2011.
3. Ammari, H., E. Iakovleva, and D. Lesselier, "A MUSIC algorithm for locating small inclusions buried in a half-space from the scattering amplitude at a fixed frequency," *SIAM Multiscale Modeling Simulation*, Vol. 3, 597–628, 2005.
4. Ammari, H., H. Kang, H. Lee, and W.-K. Park, "Asymptotic imaging of perfectly conducting cracks," *SIAM J. Sci. Comput.*, Vol. 32, 894–922, 2010.
5. Beretta, E. and E. Francini, "Asymptotic formulas for perturbations of the electromagnetic fields in the presence of thin imperfections," *Contemp. Math.*, Vol. 333, 49–63, 2003.
6. Colton, D., H. Haddar, and P. Monk, "The linear sampling method for solving the electromagnetic inverse scattering problem," *SIAM J. Sci. Comput.*, Vol. 24, 719–731, 2002.
7. Dorn, O. and D. Lesselier, "Level set methods for inverse scattering," *Inverse Problems*, Vol. 22, R67–R131, 2006.
8. Park, W.-K., "Analysis of a multi-frequency electromagnetic imaging functional for thin, crack-like electromagnetic inclusions," *Appl. Numer. Math.*, Vol. 77, 31–42, 2014.
9. Park, W.-K., "Multi-frequency subspace migration for imaging of perfectly conducting, arc-like cracks in full- and limited-view inverse scattering problems," *J. Comput. Phys.*, Vol. 283, 52–80, 2015.
10. Park, W.-K., "Subspace migration for imaging of thin, curve-like electromagnetic inhomogeneities without geometric consideration," preprint.
11. Park, W.-K. and D. Lesselier, "Electromagnetic MUSIC-type imaging of perfectly conducting, arc-like cracks at single frequency," *J. Comput. Phys.*, Vol. 228, 8093–8111, 2009.
12. Park, W.-K. and D. Lesselier, "MUSIC-type imaging of a thin penetrable inclusion from its far-field multi-static response matrix," *Inverse Problems*, Vol. 25, 075002, 2009.
13. Park, W.-K. and D. Lesselier, "Reconstruction of thin electromagnetic inclusions by a level set method," *Inverse Problems*, Vol. 25, 085010, 2009.